

RESEARCH LETTER

10.1002/2016GL072308

Key Points:

- A physical null hypothesis for the IOD is presented
- A simple low-order model captures the IOD spectrum and ENSO/IOD phase relationship
- IOD predictability is determined by ENSO predictability and ENSO signal-to-noise ratio

Supporting Information:

- Supporting Information S1

Correspondence to:

M. F. Stuecker,
stuecker@atmos.washington.edu

Citation:

Stuecker, M. F., A. Timmermann, F.-F. Jin, Y. Chikamoto, W. Zhang, A. T. Wittenberg, E. Widiasih, and S. Zhao (2017), Revisiting ENSO/Indian Ocean Dipole phase relationships, *Geophys. Res. Lett.*, *44*, 2481–2492, doi:10.1002/2016GL072308.

Received 9 DEC 2016

Accepted 27 FEB 2017

Accepted article online 2 MAR 2017

Published online 13 MAR 2017

Revisiting ENSO/Indian Ocean Dipole phase relationships

Malte F. Stuecker^{1,2,3}, Axel Timmermann^{4,5}, Fei-Fei Jin¹, Yoshimitsu Chikamoto⁶, Wenjun Zhang⁷, Andrew T. Wittenberg⁸, Esther Widiasih⁹, and Sen Zhao^{1,7}

¹Department of Atmospheric Sciences, University of Hawai'i at Mānoa, Honolulu, Hawai'i, USA, ²Department of Atmospheric Sciences, University of Washington, Seattle, Washington, USA, ³Cooperative Programs for the Advancement of Earth System Science (CPAESS), University Corporation for Atmospheric Research (UCAR), Boulder, Colorado, USA, ⁴IBS Center for Climate Physics (ICCP), Pusan National University, Busan, South Korea, ⁵IPRC, University of Hawai'i at Mānoa, Honolulu, Hawai'i, USA, ⁶Department of Plants, Soils and Climate, Utah State University, Logan, Utah, USA, ⁷Key Laboratory of Meteorological Disaster of Ministry of Education (KLME), Nanjing University of Information Science and Technology, Nanjing, China, ⁸National Oceanic and Atmospheric Administration, Geophysical Fluid Dynamics Laboratory, Princeton, New Jersey, USA, ⁹Department of Mathematics, University of Hawai'i at West O'ahu, Kapolei, Hawai'i, USA

Abstract Here we show that the characteristics of the Indian Ocean Dipole (IOD), such as its power spectrum and phase relationship with the El Niño–Southern Oscillation (ENSO), can be succinctly explained by ENSO combination mode (C-mode) wind and heat flux forcing together with a seasonal modulation of the air/sea coupled Indian Ocean (IO) Bjerknes feedback. This model explains the observed high-frequency near-annual IOD variability in terms of deterministic ENSO/annual cycle interactions. ENSO-independent IOD events can be understood as a seasonally modulated ocean response to white noise atmospheric forcing. Under this new physical null hypothesis framework, IOD predictability is determined by both ENSO predictability and the ENSO signal-to-noise ratio. We further emphasize that lead/lag correlations between different climate variables are easily misinterpreted when not accounting properly for the seasonal modulation of the underlying climate phenomena.

1. Introduction

The dominant mode of interannual climate variability is the El Niño–Southern Oscillation (ENSO), which arises from inherent dynamical instabilities in the coupled tropical air/sea system [e.g., Bjerknes, 1969; Philander, 1983; Wyrski, 1985; Cane and Zebiak, 1985; Jin and Neelin, 1993]. El Niño events are characterized by positive sea surface temperature anomalies (SSTA) in the eastern equatorial Pacific, while La Niña events exhibit negative SSTA in this region. ENSO also induces SSTA variability in the Atlantic and Indian Ocean (IO) via anomalous wind stress forcing [Latif and Barnett, 1995]. A somewhat similar mode of SSTA variability to ENSO exists in the Indian Ocean, albeit with both a weaker amplitude and smaller spatial scale. This climate mode has been termed the Indian Ocean Dipole (IOD) [Webster et al., 1999; Saji et al., 1999]. Its positive phase, which tends to be stronger than the negative phase, peaks in September–October–November (SON) and is characterized by positive SSTA in the western IO and negative SSTA in the eastern IO (Figure 1a). Coupled general circulation models (CGCMs) are generally able to simulate IOD variability, albeit with a bias toward a larger amplitude than seen in the observations [e.g., Cai and Cowan, 2013]. While some studies argue that the IOD is a largely independent mode [e.g., Webster et al., 1999; Saji et al., 1999; Iizuka et al., 2000; Behera et al., 2006], other authors demonstrate an observable influence from ENSO on the IOD [e.g., Xie et al., 2002; Annamalai et al., 2003; Krishnamurthy and Kirtman, 2003; Li et al., 2003; Loschnigg et al., 2003; Huang and Shukla, 2007; Zhang et al., 2015; Yang et al., 2015; Kajtar et al., 2016].

2. Observed IOD and ENSO Characteristics

We find that in agreement with, for instance, Loschnigg et al. [2003], only a small fraction (~32%, Figure 2a) of IOD events occur independently of ENSO events. Furthermore, the variance of ENSO and the IOD are related in the current generation of climate models [Liu et al., 2014], which indicates a close relationship between ENSO and IOD variability. The widely used CM2.1 coupled GCM [Delworth et al., 2006], despite the aforementioned larger amplitude bias of both ENSO [Wittenberg et al., 2006] and the IOD (Figure 1c), shows a realistically small fraction IOD events that are independent of ENSO (Figure 2b).

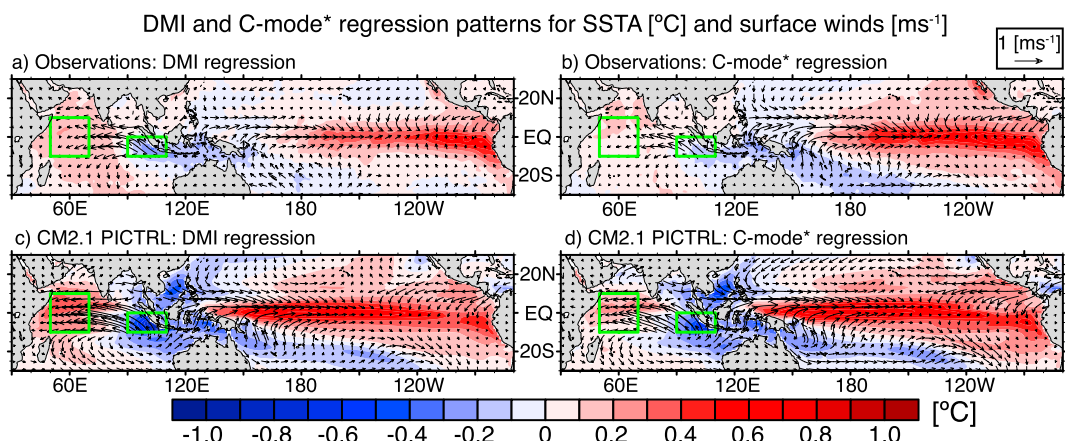


Figure 1. (a, b) Observed and (c, d) CM2.1 500 year PICTRL model regression patterns (SSTA and 10 m winds) for the normalized monthly DMI (Figures 1a and 1c) and normalized monthly C-mode* reconstruction (Figures 1b and 1d), respectively. The observational data (HadISST for SSTA and JRA-55 for surface winds) are for the period 1971–2015. The green boxes indicate the DMI index regions.

Comparing the ENSO SSTA (characterized by the N3.4 index, which denotes the area-averaged SSTA between 170°W–120°W and 5°S–5°N) in boreal summer (June–July–August: JJA) with the Dipole Mode Index (DMI), defined as the area-averaged SST anomalies in the western IO (50°E–70°E, 10°S–10°N) minus the eastern IO (90°E–110°E, 10°S–EQ), [Saji *et al.*, 1999]) during the SON season in the same year (see Figure 1 for the aforementioned regions), a high positive correlation ($R = 0.68$) is evident (Figure 2a). This relationship can be interpreted in terms of a delayed IOD response to ENSO in the preceding JJA season. A strong connection between ENSO and the IOD can also be deduced from the DMI regression pattern, which exhibits the characteristic ENSO pattern in the Pacific basin (Figure 1a).

The wide range of views regarding causality in the observed ENSO/IOD phase relationship originates partly from differing interpretations of lead/lag ENSO/IOD cross-correlation characteristics. Here we will revisit the question of causality by taking into account the different seasonal modulations of both climate phenomena.

2.1. The ENSO Combination Mode

Recent studies demonstrate that ENSO's impacts (such as low-level winds and precipitation) in the tropical and subtropical Indo-Pacific region (including the East Asian monsoon) are largely controlled by a deterministic ENSO combination mode (C-mode), which is characterized by predominantly near-annual time scales that arise from ENSO's nonlinear interactions with the climatological annual cycle [Stuecker *et al.*, 2013, 2015a, 2015b, 2016; Zhang *et al.*, 2016]. The lowest-order approximation to the theoretical C-mode can be written as [Stuecker *et al.*, 2013, 2015a]

$$C_{mode}(t) = ENSO(t) \cdot \cos(\omega_a t + \varphi_a), \quad (1)$$

where φ_a is the phase of the annual cycle influence and ω_a the frequency of the annual cycle. The C-mode represents in a compact way the seasonal modulation of ENSO's impacts as one mode. The product of ENSO (E) and the annual cycle (A) only exhibits combination tones ($A + E$ and $A - E$), but not the original frequencies (E and A): $2 \cos(A) \cos(E) = \cos(A + E) + \cos(A - E)$. An important implication is that whenever a strong annual cycle modulation exists for a climate phenomenon (such as ENSO), we immediately observe the genesis of deterministic high-frequency (predominantly near-annual) climate variability [Stuecker *et al.*, 2015b]. It has been long known that the IOD variability is strongly seasonally modulated (e.g., Xie *et al.* [2002], for a review), which is likely related to the pronounced monsoonal annual cycle in the tropical Indian Ocean [e.g., Annamalai *et al.*, 2003]. Here we revisit the ENSO-associated part of the IOD variability in light of the recently discovered tropical C-mode dynamics and in the process address the following outstanding questions regarding IOD variability.

2.2. ENSO/IOD Cross-Correlation Characteristics

The lead/lag cross-correlation between observed monthly N3.4 and the DMI exhibit some interesting features (Figure 2c): (i) The maximum positive correlation ($R = 0.39$) occurs when the IOD is leading ENSO by ~2 months. (ii) The maximum negative correlation ($R = -0.32$) occurs when the IOD is leading ENSO

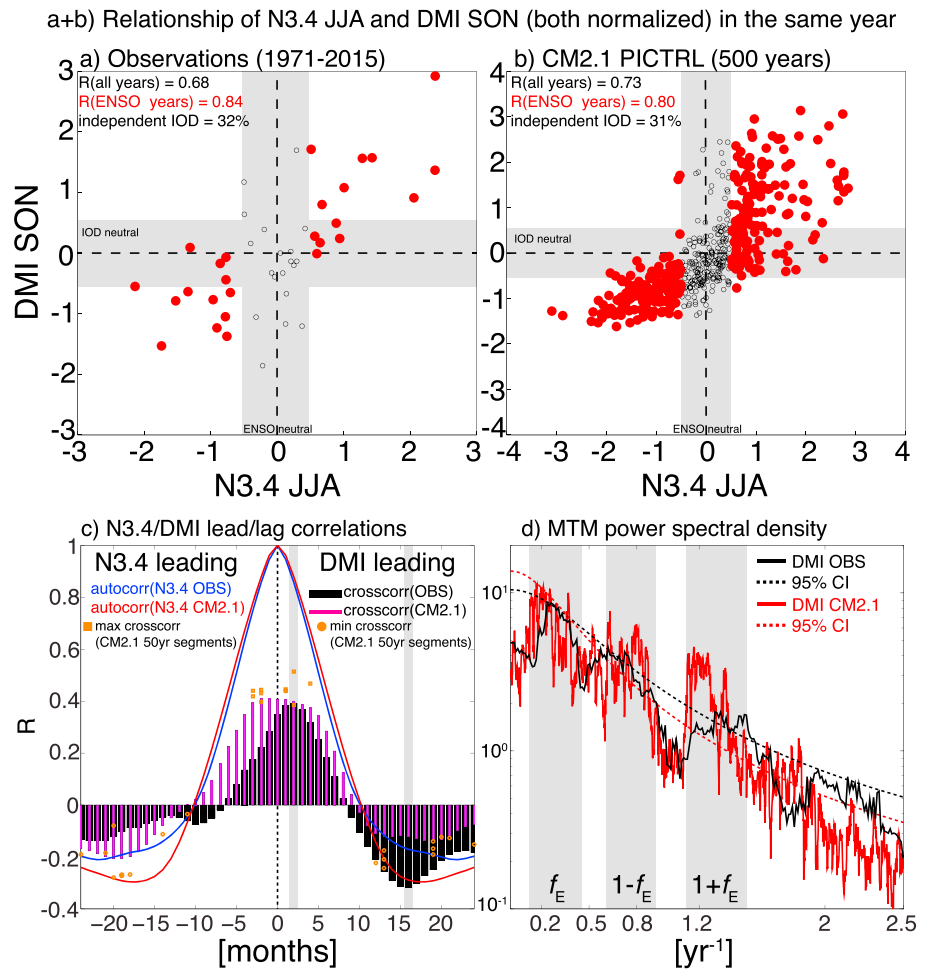


Figure 2. Relationship between the anomalous N3.4 (June–August average: JJA) and DMI (September–November average: SON) in the same year (normalized indices) for (a) the HadISST1 data (1971–2015) and (b) the CM2.1 500 year preindustrial control (PICTRL). Displayed are the linear correlations (R) for all years (black dots) and only ENSO-active years ($|N3.4 \text{ JJA}| > 0.5$; red dots). ENSO-neutral and DMI-neutral conditions are when the absolute seasonal average values are below 0.5 standard deviation (grey areas). If the year is ENSO-neutral ($|N3.4 \text{ JJA}| < 0.5$) and IOD-active ($|DMI \text{ SON}| > 0.5$), the events are classified as independent IOD. (c) Lead/lag cross-correlation between monthly N3.4 and DMI for the observations (black bars) and the CM2.1 PICTRL (magenta bars), as well as the autocorrelation for the observed N3.4 (blue line) and the CM2.1 PICTRL N3.4 (red line). Grey areas indicate the observed maximum positive and negative correlations with DMI leading N3.4. Orange squares (circles) indicate the maximum (minimum) cross-correlation values between N3.4 and DMI for 50 year segments of the CM2.1 PICTRL. (d) Multitaper method (MTM) power spectral density of the normalized monthly observed DMI (solid black line) and normalized CM2.1 PICTRL DMI (solid red line). Dashed lines indicate the 95% confidence interval (CI) for a test against an AR(1) process. Grey areas indicate the interannual ENSO frequency band (f_E), as well as the near-annual combination tones ($1 \pm f_E$).

by ~ 16 months. Here we demonstrate that the first point (i) can be easily explained by a seasonal modulation. The lead of IOD over ENSO is a result of an earlier termination of ENSO-forced IOD due to seasonal modulated air/sea coupling in the Indian Ocean. Regarding the second point (ii), *Izumo et al.* [2010] and *Jourdain et al.* [2016] interpret this IOD lead time as an ENSO response to an IOD event in the previous year (e.g., a positive IOD event in year (0) is followed by a La Niña event in year (1)). However, here we will demonstrate below that the ~ 16 month cross-correlation time scale can be largely explained by the ENSO autocorrelation time scale. Furthermore, the interpretation by *Izumo et al.* [2010] and *Jourdain et al.* [2016] neglects the different seasonal modulations of both ENSO and the IOD. If we include these, the observed characteristics are fully consistent with the following scenario: A developing El Niño in boreal summer of year 0 induces a positive IOD response in the following months. The subsequent IOD termination can be explained by the seasonal modulation of air/sea coupling processes in the Indian Ocean. Then the ENSO-induced Indian Ocean Basin (IOB) mode [e.g., *Kug et al.*, 2006; *Kug and Kang*, 2006; *Ohba and Ueda*, 2007; *Izumo et al.*, 2016] together with

the ENSO C-mode-induced southward wind shift in the Pacific basin [e.g., *McGregor et al.*, 2012; *Stuecker et al.*, 2013] will accelerate the El Niño event termination. The discharge of equatorial Pacific upper ocean heat content [*Jin*, 1997] will then subsequently lead to the development of a La Niña event in year 1. This La Niña event subsequently will induce a negative IOD event. This scenario does not require any significant ocean memory in the Indian Ocean and is fully driven by ENSO.

2.3. IOD Spectral Characteristics

It has been noted by several studies that the IOD exhibits a “biennial tendency” [e.g., *Saji et al.*, 1999] or quasi-biennial periodicities [e.g., *Ashok et al.*, 2003]. This has led to the hypothesis that the IOD might not be an independent mode but rather part of the so-called Tropospheric Biennial Oscillation (TBO) [e.g., *Meehl and Arblaster*, 2002; *Meehl et al.*, 2003]. Recent work, however, showed that for the current short observational records it is extremely difficult to reliably detect a “biennial tendency,” which uses a definition that depends on local minima and maxima in a time series (e.g., a weak monsoon year is preceded and followed by a relatively stronger monsoon year) [*Stuecker et al.*, 2015c]. Here we show that the perceived “quasi-biennial” periodicities of the IOD result, in fact, from C-mode dynamics. Importantly, the previously described “quasi-biennial” frequencies are actually near-annual when analyzing monthly data (Figure 2d), and the quasi-biennial character is largely an artifact of the deterministic high-frequency C-mode when analyzing seasonally averaged data (e.g., for the peak SON season of the IOD).

In the following manuscript sections we will demonstrate these points based on observations and CGCM experiments.

3. Data and Experiments

3.1. Observations and Model Data

For the observational period from January 1971 to December 2015 we utilize SST data from HadISST [*Rayner et al.*, 2003] and surface winds (10 m) from JRA-55 [*Kobayashi et al.*, 2015]. All anomalies are calculated with respect to the 1971–2015 climatology. Similarly, we use the SST and surface wind data from the GFDL CM2.1 preindustrial control (PICTRL) experiment [*Wittenberg*, 2009; *Wittenberg et al.*, 2014] to compare the model IOD characteristics with the observations. This model simulates an ENSO with realistic interevent diversity [e.g., *Wittenberg*, 2009; *Wittenberg et al.*, 2014], as well as the statistics of the observed ENSO/IOD relationship [*Song et al.*, 2007]. The N3.4 and DMI are calculated based on the area average definitions given in section 1.

3.2. Partially Coupled Experiments

We use the GFDL CM2.1 model to conduct a suite of partially coupled (PARCP) experiments [e.g., *Kosaka and Xie*, 2013; *Krishnamurthy et al.*, 2015; *Yang et al.*, 2015]. The atmosphere component is forced by prescribed SSTs (climatology plus anomalies) in the tropical eastern Pacific, while full air/sea coupling is allowed everywhere else (see Figure S1 in the supporting information). In the ENSO forcing region, a 5 day damping time scale is used to prescribe the SSTs. In the first experiment we conduct an ensemble ($n=30$) with idealized 1997–1999 ENSO SSTA forcing to test whether we are able to simulate the observed monthly IOD evolution when the ENSO forcing is prescribed. The second ensemble ($n=15$) is forced by a realistic ENSO regression pattern in the eastern equatorial Pacific [*Stuecker et al.*, 2015a, Figure 2] with an idealized 2.5 year sinusoidal time evolution. The ensemble is conducted by starting from one initial condition and repeating the 2.5 year sinusoidal ENSO and the 1997–1999 event, respectively. It has been shown in *Stuecker et al.* [2015a, 2015b] that this idealized forcing provides a powerful way to diagnose the nonlinear C-mode time scale interactions as well as their remote influences on the climate system. These experiments complement the partially coupled ocean mixed layer experiments conducted in *Stuecker et al.* [2015a], with the difference of a fully dynamical ocean that allows for coupled air/sea dynamics in the Indian Ocean.

4. Simple IOD Models and Coupled GCM Experiment Results

4.1. A Stochastic Null Hypothesis Model for the IOD

In the absence of any ENSO forcing, our null hypothesis for the IOD is a stochastically forced model with a seasonally varying damping rate [*de Elvira and Lemke*, 1982; *Nicholls*, 1984], which is an extension of the original stochastic climate model [*Hasselmann*, 1976; *Frankignoul and Hasselmann*, 1977]:

$$\frac{dT}{dt} = [-\lambda_0 + \lambda_a \cos(\omega_a t + \varphi_l)] T(t) + \xi(t), \quad (2)$$

where dT/dt is the temperature tendency for the DMI and ξ is white noise heat flux forcing (weather). We choose a mean SSTA damping rate λ_0 value of $1/2 \text{ month}^{-1}$ and the damping rate annual cycle λ_a value of $1/4 \text{ month}^{-1}$, respectively, which are realistic values for SSTA damping in the Indian Ocean (as long as $\lambda_a \leq \lambda_0$, we are in a stable damped regime). The phase for the damping rate annual cycle φ_l is chosen so that we have a minimum of the annual cycle ($\cos(\omega_a t + \varphi_l)$) in April and a maximum in October. These values are chosen as Annamalai *et al.* [2003] showed that the annual cycles of Eastern Equatorial Indian Ocean (EEIO) convection, ocean barrier layer thickness, thermocline depth, and Indonesian Throughflow transport in boreal spring are all most conducive to amplify perturbations of the coupled system, thereby creating a time window during which the IOD is most sensitive to external forcing (due to the seasonally varying feedback efficiency in the damping term). For these values equation (2) already produces a red spectrum [de Elvira and Lemke, 1982] as well as the observed IOD seasonal variance modulation (not shown), exhibiting a maximum amplitude in boreal fall (SON) and minimum in boreal spring (MAM) without the requirement of an oscillation. Therefore, white noise forcing with a seasonally modulated damping rate is sufficient to explain the statistics of ENSO-independent IOD events (Figures 2a and 2b).

4.2. ENSO-Forced IOD Model

Next, we consider the response of the Indian Ocean SST to ENSO forcing: The ENSO-forced 1997–1999 PARCP experiment ensemble mean simulates very well the monthly evolution of the observed DMI (Figure 3a, $R = 0.93$), supporting the hypothesis that the IOD is largely a forced response to ENSO. Not only do we simulate the positive IOD event in 1997 and the negative IOD event in 1998 with their maximum amplitude in the SON season, we also capture the higher frequency variability that is evident in the monthly evolution of the DMI. The fact that the IOD response exhibits higher frequency variability than the ENSO time scale is also clearly evident in the 2.5 year sinusoidal ENSO PARCP experiment (Figure 3b). To explain the origin of this shorter time scale, we expand our simple IOD model (equation (2)) so that we consider a seasonally modulated ENSO forcing (equation (1)):

$$\frac{dT}{dt} = [-\lambda_0 + \lambda_a \cos(\omega_a t + \varphi_l)] T(t) - \beta N3.4(t) \cos(\omega_a t + \varphi_a) + \xi(t), \quad (3)$$

where T is now the integrated C-mode effect (referred to as C-mode* here) and β a scaling coefficient (for simplicity it is set to one here and we analyze normalized indices in this paper). Note that the ratio of the forcing and the feedback terms will impact the amplitude of the individual peaks in the power spectra. We submit the idea that C-mode* is an excellent approximation of the DMI. For simplicity, we neglect the ENSO-independent random forcing ($\xi(t) = 0$) in the remaining manuscript and treat equation (3) as a deterministic equation. As the EEIO SSTA are dynamically connected with the western equatorial Indian Ocean via the Bjerknes feedback [Bjerknes, 1969], we chose that our model represents the zonal IO SSTA gradient (as described by the DMI). To be consistent with previous studies, we use the notation that a positive T corresponds to a positive IOD event. As positive IOD events are associated with negative SSTA in the eastern IO, we use a C-mode forcing in this equation that is of opposite sign as in Stuecker *et al.* [2013, 2015a]. The phase for the ENSO modulation annual cycle φ_a is chosen so that we have a maximum of the annual cycle in March and a minimum in September. This seasonal modulation of the forcing is motivated by previous research that highlighted the importance of the C-mode (the seasonally modulated ENSO signal) in shaping the anomalous atmospheric circulation in the Indo-Pacific region [Stuecker *et al.*, 2013, 2015a, 2015b]. Applying this simple model (3) for the 1997–1999 case and the 2.5 year sinusoidal N3.4 forcing ($T = \text{C-mode}^*$, see Appendix A and Text S1 in the supporting information), we find a very high correlation with the CGCM-simulated ensemble mean DMI ($R = 0.93$ for the 1997–1999 experiment and $R = 0.88$ for the 2.5 year sinusoidal ENSO experiment; Figures 3a and 3b). Even for the full time series (not ensemble mean), we find very high correlations between the analytical solution to equation (3) with the respective SST forcing and the DMI for both the 1997–1999 experiment ($R = 0.84$) and the 2.5 year sinusoidal ENSO experiment ($R = 0.75$), thus suggesting that most of the CM2.1 IOD events are indeed ENSO forced and seasonally terminated. This simple model is sufficient to capture the simulated monthly IOD time evolution. Furthermore, the observed and simulated amplitude difference between boreal spring (MAM) and boreal fall (SON) in the IOD variance can be succinctly captured by the seasonally varying damping rate in the model (equation (3)). The physical basis for this model is that the anomalous surface wind stress and heat fluxes induced by the atmospheric ENSO C-mode circulation in the eastern Indian Ocean are represented by the right-hand side forcing term in equation (3). It can be seen in Zhang *et al.* [2016] that the C-mode-induced C-mode SSTA pattern shows a dipole structure in the Indian Ocean with distinct SSTA cooling in the eastern basin during the boreal summer season of a developing El Niño event.

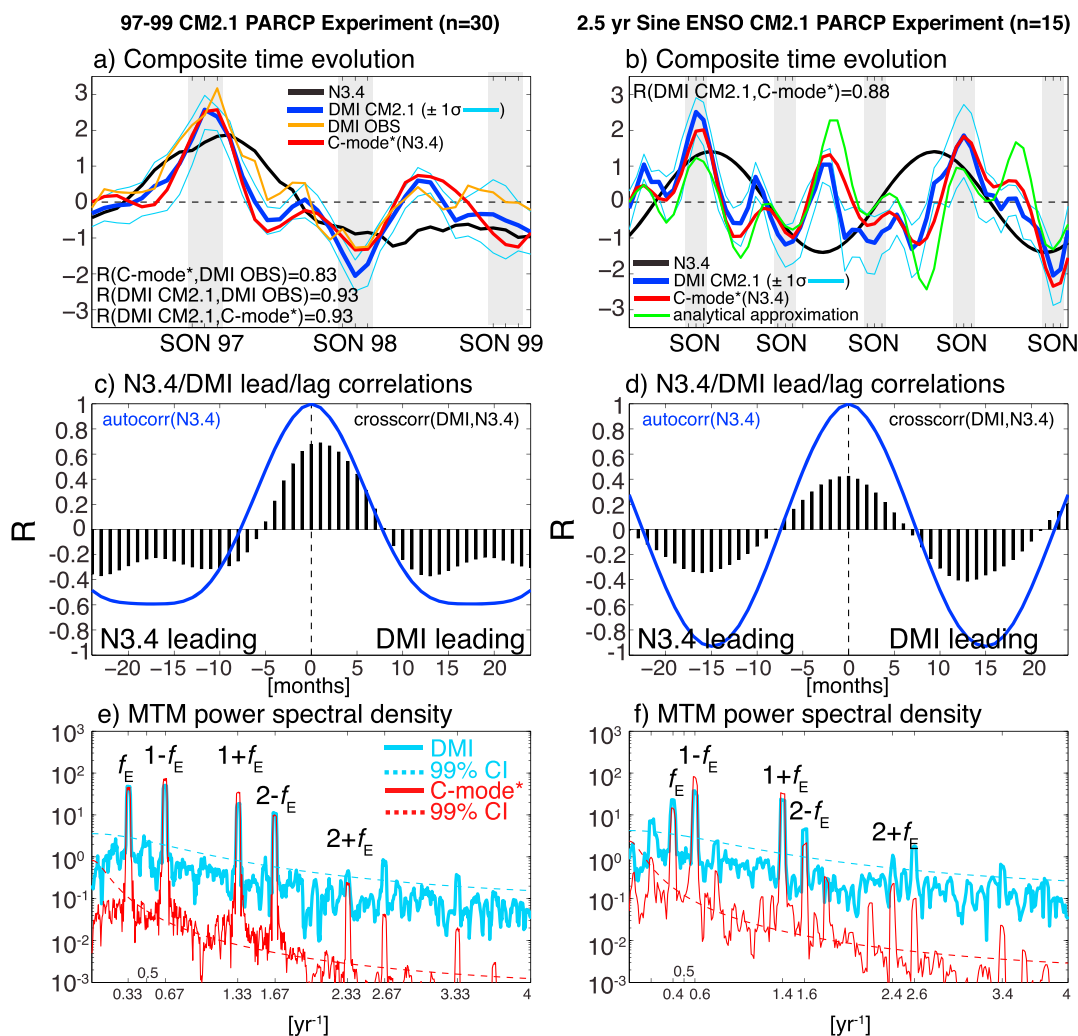


Figure 3. Results from the CM2.1 PARCP experiments: Repeated (left column) 1997–1999 ENSO event (30 ensemble members) and (right column) 2.5 year sinusoidal ENSO (15 ensemble members). (a, b) Ensemble mean time evolution of the normalized N3.4 forcing (black line), normalized DMI response (blue line with 1 standard deviation spread as thin cyan lines), and normalized theoretical integrated C-mode* (red line). Additionally, the observed normalized DMI is shown for the 1997–1999 event (orange line) and the approximate analytical solution (green line, equation (A2)) for the 2.5 year experiment. (c, d) Lead/lag correlations between the full time series (not ensemble mean) monthly N3.4 and DMI indices (black bars), as well as the autocorrelation for the N3.4 forcing (blue line) for the respective CM2.1 partially coupled simulations. (e, f) MTM power spectral density (no unit) of the full time series (not ensemble mean) of monthly normalized DMI (solid cyan line) and the normalized C-mode* (solid red line) from the CM2.1 partially coupled simulations. Dashed lines indicate the 99% confidence intervals (CI) when tested against AR(1) processes. The interannual ENSO forcing frequency (f_E), as well as the near-annual ($1 \pm f_E$) and near-semiannual ($2 \pm f_E$) combination tones are labeled. The forcing frequency is the repeating 3 year segment (1997–1999) in Figure 3e.

4.3. Experiment IOD Spectral Characteristics

The power spectra (using the multitaper method (MTM) [e.g., Ghil et al., 2002]) exhibit clearly the annual and semiannual cycle combination tones ($1 \pm f_E$ and $2 \pm f_E$; for a full discussion of the nonlinear combination tone genesis, refer to Stuecker et al. [2015b]), which explain the observed (Figure 2d) and simulated (cyan lines in Figures 3e and 3f) near-annual and subannual variations of the IOD, as well as the ENSO frequency f_E in the IOD response. All these peaks stand clearly out of the background noise level (the full simulated time series is used to calculate the spectra, not the ensemble mean). As our conceptual IOD models (equations (2) and (3)) include the integrated effect of air/sea interactions, we choose a statistical significance test against an AR(1) process [Hasselmann, 1976; Frankignoul and Hasselmann, 1977; Frankignoul, 1985] as our statistical null hypothesis (Figures 2d, 3e, and 3f).

The spectrum of the C-mode* reconstruction of the IOD (red lines in Figures 3e and 3f) captures the simulated spectrum very well. Even though the forcing only contains the near-annual $1 \pm f_E$ combination tones (Figure S2b), we observe the genesis of both the ENSO frequency f_E and the semiannual $2 \pm f_E$ combination tones in the integrated C-mode* response (Figures 3e and 3f). This can be explained by frequency unfolding due to the interaction of the C-mode forcing with the seasonally varying damping rate ($\lambda_a \cdot \cos(\omega_a t - \varphi_1)$). The original interannual ENSO frequencies (E) are unfolded by the second seasonal modulation (through the damping rate) of the seasonally modulated ENSO forcing signal ($A + E$ and $A - E$). The analytical solution of equation (3) (see Appendix A and Text S1) exhibits additional to the C-mode forcing time scales $1 \pm f_E$, the ENSO time scale f_E , the semiannual cycle combination tones $2 \pm f_E$, and low-amplitude higher-order combination tones (see Appendix A and Text S1). When no seasonal cycle in the damping rate is considered ($\lambda_a = 0$), only the ENSO C-mode forcing frequencies $1 \pm f_E$ are evident in the integrated C-mode* response (Figure S2d), with a slight reddening toward the lower frequency difference tone ($1 - f_E$). On the other hand, the purely stochastic IOD model with a seasonally varying damping rate (equation (2)) generates a red spectrum without any spectral peaks (Figure S2f). Summarizing, our deterministic IOD model (equation (3)) is consistent with the observed DMI spectrum (Figure 2d), which exhibits pronounced variability both at the ENSO frequency and the near-annual combination tones. Importantly, the ENSO-forced IOD model (equation (3)) is sufficient to cause biennial characteristics when comparing, for instance, year-to-year seasonal averages instead of a monthly time evolution. The smallest time scale that can be resolved with an annual sampling is a signal with a 2 year period (Nyquist frequency). Thus, near-annual deterministic C-mode time scales can easily be misinterpreted as “biennial tendency” and the quasi-biennial periodicities discussed in the previous literature.

4.4. ENSO/IOD Cross-Correlation Characteristics

Next, we investigate the observed ENSO/IOD cross-correlation characteristics (Figure 2c). As mentioned before, the observed DMI exhibits the largest correlation with ENSO with 2 months (for largest positive correlation) and 16 months (for largest negative correlation) lead times. The CM2.1 PICTRL approximately captures this cross-correlation relationship (magenta bars in Figure 2c). However, when looking at individual 50 year time slices of the CM2.1 PICTRL (orange symbols in Figure 2c) we can see that the exact lead times are sensitive to individual sampling periods, with some periods displaying a leading DMI, while others display a leading ENSO. Importantly, the observed 2 months lead time of DMI can clearly be attributed to the different seasonal modulations of the two phenomena: ENSO is peaking in boreal winter, while the IOD is peaking in boreal fall. Previous studies [Izumo *et al.*, 2010; Jourdain *et al.*, 2016] interpret the longer negative lead time of the IOD as an indication for a delayed ENSO response to an IOD forcing in the preceding year. Furthermore, it is striking that the ENSO autocorrelation function (blue line) displays a very similar character to the ENSO/IOD cross-correlation (black bars), leading us to hypothesize that the ~ 16 months lead time of the negative IOD/ENSO correlation might in fact just be the statistical ENSO autocorrelation signal that has been transferred to the ENSO-induced IOD response (as captured by C-mode*). Indeed, in our idealized partially coupled CM2.1 experiments the IOD response clearly shows the same cross-correlation characteristics with the ENSO forcing (Figures 3c and 3d). The same is the case for the analytical ENSO/C-mode* cross-correlation (Figure S2a). Again, the frequency unfolding of the C-mode forcing through the seasonally varying damping rate (equation (3)) explains how an ENSO autocorrelation can produce the observed ENSO/IOD cross correlation. Note that by including noise into equation (3), the maximum amplitude of the correlation becomes more realistic. Additionally, any direct linear (nonmodulated) interannual ENSO forcing will further augment this cross-correlation, especially the quasi-biennial (QB) ENSO time scale [e.g., Bejarano and Jin, 2008]. Thus, we argue that the observed ENSO/IOD cross-correlation relationship is not necessarily indicative of the IOD forcing ENSO, since it is also clearly consistent with seasonally modulated ENSO forcing the seasonally modulated IOD. This illustrates that interpreting seasonal lead/lag relationships in terms of causality, without fully accounting for the seasonal characteristics of the signals can lead to ambiguities and inconsistencies. Importantly, it does not rule out that Indian Ocean SSTA assist the ENSO event termination as demonstrated in many previous studies [e.g., Kug *et al.*, 2006; Kug and Kang, 2006; Ohba and Ueda, 2007; Izumo *et al.*, 2016]. These diagnosed cross-correlation characteristics do not exist if either the seasonally modulated damping rate is absent in the deterministic C-mode forced model (Figure S2c) or if we only consider white noise forcing with a seasonally modulated damping rate (Figure S2e). Furthermore, individual stochastic ENSO-independent extreme IOD events could, on occasion, induce ENSO events [Luo *et al.*, 2010], which could further contribute to the observed ENSO/IOD cross-correlation characteristics.

4.5. Observations and CM2.1 Preindustrial Control

Next, we use equation (3) to compare our IOD reconstruction with the observations and the CM2.1 preindustrial control. Both λ_0 and λ_a have the same values as previously mentioned, and the phase for the ENSO modulation annual cycle φ_a is chosen so that we have a maximum of the annual cycle in February and a minimum in August (as in *Stuecker et al.* [2013, 2015a]), consistent with the statistics of the CM2.1 model. The results are qualitatively similar when using the same annual cycle phase as before. Deviations in the annual cycle phases by about 1 month between observations and coupled models can be expected due to model seasonal cycle biases.

As expected, when forcing equation (3) with the observed N3.4 from 1971 to 2015, we find a good lag 0 linear correlation ($R = 0.46$) between the observed monthly DMI and the ENSO-forced simple IOD model. An even higher lag 0 correlation is observed between the DMI in the 500 year CM2.1 PICTRL and the C-mode* reconstruction ($R=0.51$) if equation (3) is forced with the simulated N3.4 from the CM2.1 simulation. During ENSO-neutral periods the short-memoried IOD would be noise driven, thus explaining correlation values smaller than in our ENSO-forced CM2.1 experiments. As a result, when considering only ENSO-active periods (Figure S3), the correlation between the observed IOD and the reconstruction significantly improves. Our model effectively captures the observed evolution for both La Niña periods (e.g., Figure S3a) and El Niño periods (e.g., Figures S3b and S3d). When contrasting the 1982/1983 (Figure S3b) and 1997/1998 (Figure S3d) events, it can be seen that our damping time scale estimate is a good fit for the 1982/1983 event but slightly too short for the 1997/1998 event. While most IOD events can be attributed to ENSO C-mode forcing, some events (such as the 1994 IOD, Figure S3c) might be noise induced (especially during ENSO-neutral periods) as described by our stochastic IOD model (equation (2)). Additionally, it was hypothesized that the 1994 IOD event played a role in shaping the 1994 El Niño [*Luo et al.*, 2010]. Finally, both the C-mode* reconstruction SST and surface wind regression patterns for the observations (Figure 1b) and the CM2.1 PICTRL (Figure 1d) exhibit very similar spatial structures to the patterns associated with the IOD indices (Figures 1a and 1c), thus supporting our simple model formulation (equation (3)).

5. Discussion and Conclusions

In the present study we propose a simple physical null hypothesis for the IOD. Most of the IOD events can be explained as the integrated response to a seasonally modulated ENSO forcing (C-mode) with a seasonally modulated damping rate (equations (3) and (A1)). The remaining ENSO-independent IOD events can be sufficiently captured by the integrated effect of white noise forcing with a seasonally modulated damping rate (equation (2)). Therefore, no Indian Ocean oscillatory mechanism (other than ENSO and the seasonal cycle) is required to explain the observed IOD events. Furthermore, we are able to explain the observed IOD spectrum and ENSO/IOD cross-correlation characteristics with these simple models. Even though in our model the forcing occurs only on near-annual C-mode time scales with short autocorrelation time scale, the further modulation through the seasonally varying SST damping rate causes frequency unfolding and creates additionally the ENSO frequency and the semiannual combination tones in the IOD response. Thus, we also find the ENSO autocorrelation information in the IOD variables, which causes an apparent ~ 16 months lead time of the positive IOD ahead of La Niña; but which is actually caused by (i) a 2 month lead of seasonally modulated El Niño forcing ahead of the positive IOD and (ii) the tendency for El Niño events to be followed ~ 14 months later by La Niña. Furthermore, the nonsinusoidal nature of the monsoonal annual cycle could likely be responsible for the genesis of higher-order combination tones and will be investigated in a future study.

These results have important implications for the predictability of IOD events: Once we observe a developing El Niño event in boreal spring and summer, it likely forces a positive IOD event to boreal fall of year 0 (SON) via the atmospheric ENSO C-mode circulation in the Indian Ocean. Meanwhile, in the Pacific the atmospheric C-mode [*McGregor et al.*, 2012; *Stuecker et al.*, 2013, 2015a, 2016] and the Indian Ocean-induced Walker circulation changes [e.g., *Kug et al.*, 2006; *Kug and Kang*, 2006; *Ohba and Ueda*, 2007; *Izumo et al.*, 2016] can contribute to a rapid termination of the El Niño event in boreal winter and the subsequent transition to a La Niña state in the eastern equatorial Pacific. Thus, in the following year 1 SON we observe a negative IOD response (Eastern Indian Ocean warming) to the La Niña forcing. Importantly, no long-term ocean-dynamical memory in the Indian Ocean is required for this mechanism. This suggests potential predictability beyond 1 year once an

El Niño event is in its growth phase in late boreal spring to early boreal summer. However, during ENSO-neutral periods we expect little potential predictability of the IOD, given that these independent events are likely noise forced with a much shorter damping time scale than air/sea coupled dynamics in the eastern equatorial Pacific.

The dynamics of the IOD and their interaction with ENSO in the Pacific likely vary much across different CGCMs—from highly damped IODs (excited by either noise or ENSO) to oscillatory regimes (with a distinct IOD frequency), and from strong to weak interbasin connections. The sensitivity of Pacific/Indian Ocean feedbacks would need to be addressed in partially coupled experiments for a large sample of different models, each with their distinct mean state and annual cycle biases. As the statistics of the ENSO/IOD relationship are comparable between the observations and CM2.1 (e.g., the percentage of independent IOD events) we have confidence that the diagnosed relationship is realistic. From our results, we further conclude that IOD predictability depends crucially on ENSO predictability and the ENSO signal-to-atmospheric-noise ratio in the Indian Ocean. Furthermore, the IOD seasonal synchronization is largely caused by the annual cycle of the damping rate. The physical processes responsible for the seasonal modulation of the EEIO damping rate have been explored by *Annamalai et al.* [2003]. We have demonstrated that the dominant near-annual timescales of the IOD could be driven by the first-order ENSO C-mode forcing. On the other hand, the basin-wide IO warming (the aforementioned IOB mode) [*Xie et al.*, 2009] might be more affected by the direct linear ENSO response (with a delay), with the seasonal modulation playing a second-order role.

It is important to note that the projected (and already detected [*Knutson et al.*, 2013]) mean state changes in the Indian Ocean favor enhanced future occurrences of extreme (from an atmospheric perspective) IOD events [*Cai et al.*, 2014a]. At the same time the occurrence of extreme El Niño events (also from an atmospheric perspective) is also projected to increase, in response to greenhouse warming [*Cai et al.*, 2014b]. As a large fraction of IOD events is forced by ENSO, both the effect of Indian Ocean mean state changes [*Cai et al.*, 2014a] and the increase of extreme El Niño events [*Cai et al.*, 2014b] are conducive for a future increase of IOD events and a persistence of the ENSO/IOD linkage via extended combination mode dynamics in a warmer future world. Indeed, it has been shown previously that zonal South Pacific Convergence Zone (SPCZ) events are projected to increase in response to greenhouse warming [*Cai et al.*, 2012], which are a manifestation of the ENSO C-mode in the Pacific basin [*Stuecker et al.*, 2013]. All these factors suggest that the characteristics of the ENSO/IOD relationship as proposed here are likely to continue in the future. Furthermore, as ENSO and its predictability are intrinsically modulated on decadal time scales [e.g., *Wittenberg*, 2009; *Wittenberg et al.*, 2014; *Karamperidou et al.*, 2014], our hypothesis implies that the IOD will be as well—even without considering any changes in the climate mean state.

Moreover, it has been shown that the Indian Ocean, in general, and the IOD, specifically, exhibit global teleconnections [e.g., *Saji and Yamagata*, 2003; *Nuncio and Yuan*, 2015], the latter of which are in fact largely part of the extended seasonally modulated and integrated ENSO signal. Thus, ENSO might have a larger effect on climate variability in the extratropics than previously thought. A caveat to consider are considerable mean state, annual cycle, and climate variability biases that are still evident in the current generation of climate models, implying that the exact strength of the proposed ENSO/IOD relationship might differ significantly between observations and different models. Importantly, previous work on the extension of ENSO's impacts [*Stuecker et al.*, 2013, 2015a, 2015b, 2016; *Zhang et al.*, 2016] together with the results presented here strongly suggest that strong emphasis should be given to reduce model biases in the simulation of ENSO and the tropical annual cycles. Given the prominent role of ENSO in the climate system, we would then expect many other ENSO-dependent modes of climate variability (such as the IOD) to improve as well.

Appendix A: Analytical Solution for the Deterministic IOD Model

The observed spectral and cross-correlation characteristics of the IOD can be explained by the time scales generated by our simple deterministic IOD model (equation (3) without noise). For simplicity, we assume a sinusoidal ENSO forcing with frequency ω_0 and phase φ_0 to simplify equation (3):

$$\frac{dT}{dt} = T'(t) = [-\lambda_0 + \lambda_a \cos(\omega_a t + \varphi_1)] T(t) - \cos(\omega_0 t + \varphi_0) \cos(\omega_a t + \varphi_a). \quad (A1)$$

It can be shown (full derivation with the variable and parameter definitions can be found in Text S1 in the supporting information) that the approximate analytical solution \tilde{T} (using a Taylor series expansion with error $O(\epsilon^2)$) has the following form when separated into terms according to their time scales:

$$\begin{aligned}
 \tilde{T}(t) = & - \overbrace{\frac{1}{\sqrt{\lambda_0^2 + \omega_a^2}} [\cos(\omega_a t - \theta_0^\# + \varphi_a) \cos(\omega_0 t + \varphi_0)]}^{1 \pm f_E} \\
 & - \overbrace{\frac{\epsilon}{2\sqrt{\lambda_0^2 + \omega_a^2}} [\sin(\varphi_l - \varphi_a + \theta_0^\#) \cos(\omega_0 t + \varphi_0)]}^{f_E} \\
 & - \overbrace{\frac{\epsilon}{2\sqrt{\lambda_0^2 + \omega_a^2}} [\sin(2\omega_a t + \varphi_a + \varphi_l - \theta_0^\#) \cos(\omega_0 t + \varphi_0)]}^{2 \pm f_E} \\
 & - \overbrace{\frac{\epsilon}{2\sqrt{\lambda_0^2 + 2\omega_a^2}} [\sin(2\omega_a t + \theta_1^\# + 2\varphi_a) \cos(\omega_0 t + \varphi_0)]}^{2 \pm f_E}.
 \end{aligned} \tag{A2}$$

Hence, the seasonally modulated damping rate is responsible for the frequency unfolding from the C-mode forcing ($1 \pm f_E$) to a response that includes both the ENSO time scale (f_E) and the semiannual combination tones ($2 \pm f_E$) additional to the C-mode time scale. The neglected higher-order terms of the Taylor series expansion would further correct the amplitudes of the existing terms as well as create additional higher-frequency terms (such as $3 \pm f_E$). The error estimate of the approximation as a function of λ_a is shown in Figure S4.

Acknowledgments

This research was supported by the NOAA Climate and Global Change Postdoctoral Fellowship Program, administered by UCAR's Cooperative Programs for the Advancement of Earth System Sciences (CPAESS). Additionally, this study was partially supported by U.S. NSF grant AGS-1406601, U.S. Department of Energy grant DE-SC0005110, the Institute for Basic Science (project code IBS-R028-D1), and the SOA Program on Global Change and Air-Sea Interactions (GASI-IPOVAI-03). This is SOEST publication 9979 and ICCP publication 1. We thank J.-S. Kug and one anonymous reviewer for their valuable comments. M.F.S. thanks Sarah Post for insightful discussions and GFDL for support and resources during a research visit. The data used in this study can be obtained from the corresponding author.

References

- Annamalai, H., R. Murtugudde, J. Potemra, S.-P. Xie, P. Liu, and B. Wang (2003), Coupled dynamics over the Indian Ocean: Spring initiation of the zonal mode, *Deep Sea Res., Part II*, *50*, 2305–2330, doi:10.1016/S0967-0645(03)00058-4.
- Ashok, K., Z. Guan, and T. Yamagata (2003), A look at the relationship between ENSO and the Indian Ocean Dipole, *J. Meteorol. Soc. Jpn.*, *81*, 41–56.
- Behera, W. K., J. J. Luo, S. Masson, S. A. Rao, H. Sakuma, and T. Yamagata (2006), A CGCM study on the interaction between IOD and ENSO, *J. Clim.*, *19*, 1688–1705.
- Bejarano, L., and F.-F. Jin (2008), Coexistence of equatorial coupled modes of ENSO, *J. Clim.*, *21*, 3051–3067, doi:10.1175/2007JCLI1679.1.
- Bjerknes, J. (1969), Atmospheric teleconnections from the equatorial Pacific, *Mon. Weather Rev.*, *97*, 163–172.
- Cai, W., and T. Cowan (2013), Why is the amplitude of the Indian Ocean Dipole overly large in CMIP3 and CMIP5 climate models?, *Geophys. Res. Lett.*, *40*, 1200–1205, doi:10.1002/grl.50208.
- Cai, W., et al. (2012), More extreme swings of the South Pacific convergence zone due to greenhouse warming, *Nature*, *488*, 365–369, doi:10.1038/nature11358.
- Cai, W., A. Santoso, G. Wang, E. Weller, L. Wu, K. Ashok, Y. Masumoto, and T. Yamagata (2014a), Increased frequency of extreme Indian Ocean Dipole events due to greenhouse warming, *Nature*, *510*, 254–258, doi:10.1038/nature13327.
- Cai, W., et al. (2014b), Increasing frequency of extreme El Niño events due to greenhouse warming, *Nat. Clim. Change*, *4*, 111–116, doi:10.1038/nclimate2100.
- Cane, M. A., and S. E. Zebiak (1985), A theory for El Niño and the Southern Oscillation, *Science*, *228*, 1085–1087, doi:10.1126/science.228.4703.1085.
- de Elvira, A. R., and P. Lemke (1982), A Langevin equation for stochastic climate models with periodic feedback and forcing variance, *Tellus*, *34*, 313–320.
- Delworth, T. L., et al. (2006), GFDL's CM2 global coupled climate models. Part I: Formulation and simulation characteristics, *J. Clim.*, *19*, 634–674, doi:10.1175/JCLI3629.1.
- Frankignoul, C. (1985), Sea surface temperature anomalies, planetary waves, and air-sea feedback in the middle latitudes, *Rev. Geophys.*, *23*, 357–390.
- Frankignoul, C., and K. Hasselmann (1977), Stochastic climate models, Part II. Application to sea-surface temperature anomalies and thermocline variability, *Tellus*, *29*, 289–305, doi:10.1111/j.2153-3490.1977.tb00740.x.
- Ghil, M., et al. (2002), Advanced spectral methods for climatic time series, *Rev. Geophys.*, *40*(1), 1003, doi:10.1029/2000RG000092.
- Hasselmann, K. (1976), Stochastic climate models Part I. Theory, *Tellus*, *28*, 473–485, doi:10.1111/j.2153-3490.1976.tb00696.x.
- Huang, B., and J. Shukla (2007), Mechanisms for the interannual variability in the Tropical Indian Ocean. Part I: The role of remote forcing from the Tropical Pacific, *J. Clim.*, *20*, 2917–2936, doi:10.1175/JCLI4151.1.
- Iizuka, S., T. Matsuura, and T. Yamagata (2000), The Indian Ocean SST dipole simulated in a coupled general circulation model, *Geophys. Res. Lett.*, *27*, 3369–3372, doi:10.1029/2000GL011484.
- Izumo, T., J. Vialard, M. Lengaigne, C. de Boyer Montegut, S. K. Behera, J.-J. Luo, S. Cravatte, S. Masson, and T. Yamagata (2010), Influence of the state of the Indian Ocean Dipole on the following year's El Niño, *Nat. Geosci.*, *3*, 168–172, doi:10.1038/ngeo760.
- Izumo, T., J. Vialard, H. Dayan, M. Lengaigne, and I. Suresh (2016), A simple estimation of equatorial Pacific response from windstress to untangle Indian Ocean Dipole and Basin influences on El Niño, *Clim. Dyn.*, *46*, 2247–2268, doi:10.1007/s00382-015-2700-4.

- Jin, F.-F. (1997), An equatorial ocean recharge paradigm for ENSO. Part I: Conceptual model, *J. Atmos. Sci.*, *54*, 811–829.
- Jin, F.-F., and J. D. Neelin (1993), Modes of interannual tropical ocean-atmosphere interaction—A unified view. Part I: Numerical results, *J. Atmos. Sci.*, *50*, 3477–3503.
- Jourdain, N. C., M. Lengaigne, J. Vialard, T. Izumo, and A. S. Gupta (2016), Further insights on the influence of the Indian Ocean Dipole on the following year's ENSO from observations and CMIP5 models, *J. Clim.*, *29*, 637–658, doi:10.1175/JCLI-D-15-0481.1.
- Kajtar, J. B., A. Santoso, M. H. England, and W. Cai (2016), Tropical climate variability: Interactions across the Pacific, Indian, and Atlantic Oceans, *Clim. Dyn.*, doi:10.1007/s00382-016-3199-z.
- Karamperidou, C., M. A. Cane, U. Lall, and A. T. Wittenberg (2014), Intrinsic modulation of ENSO predictability viewed through a local Lyapunov lens, *Clim. Dyn.*, *42*, 253–270, doi:10.1007/s00382-013-1759-z.
- Knutson, T. R., F. Zeng, and A. T. Wittenberg (2013), Multimodel assessment of regional surface temperature trends: CMIP3 and CMIP5 twentieth-century simulations, *J. Clim.*, *26*, 8709–8743, doi:10.1175/JCLI-D-12-00567.1.
- Kobayashi, S., et al. (2015), The JRA-55 reanalysis: General specifications and basic characteristics, *J. Meteorol. Soc. Jpn.*, *93*, 5–48, doi:10.2151/jmsj.2015-001.
- Kosaka, Y., and S.-P. Xie (2013), Recent global-warming hiatus tied to equatorial Pacific surface cooling, *Nature*, *501*, 403–407, doi:10.1038/nature12534.
- Krishnamurthy, L., G. A. Vecchi, R. Msadek, A. Wittenberg, T. L. Delworth, and F. Zeng (2015), The seasonality of the great plains low-level jet and ENSO relationship, *J. Clim.*, *28*, 4525–4544, doi:10.1175/JCLI-D-14-00590.1.
- Krishnamurthy, V., and B. Kirtman (2003), Variability of the Indian Ocean: Relation to monsoon and ENSO, *Q. J. R. Meteorol. Soc.*, *129*, 1623–1646, doi:10.1256/qj.01.166.
- Kug, J.-S., and I.-S. Kang (2006), Interactive feedback between the Indian Ocean and ENSO, *J. Clim.*, *19*, 1784–1801, doi:10.1175/JCLI3660.1.
- Kug, J.-S., T. Li, S.-I. An, I.-S. Kang, J.-J. Luo, S. Masson, and T. Yamagata (2006), Role of the ENSO-Indian Ocean coupling on ENSO variability in a coupled GCM, *Geophys. Res. Lett.*, *33*, L09710, doi:10.1029/2005GL024916.
- Latif, M., and T. P. Barnett (1995), Interactions of the tropical oceans, *J. Clim.*, *8*, 952–964.
- Li, T., B. Wang, C.-P. Chang, and Y. Zhang (2003), A theory for the Indian Ocean Dipole—Zonal mode, *J. Atmos. Sci.*, *60*, 2119–2135.
- Liu, L., S.-P. Xie, X.-T. Zheng, T. Li, Y. Du, G. Huang, and W.-D. Yu (2014), Indian Ocean variability in the CMIP5 multi-model ensemble: The zonal dipole mode, *Clim. Dyn.*, *43*, 1715–1730, doi:10.1007/s00382-013-2000-9.
- Loschnigg, J., G. A. Meehl, P. J. Webster, J. M. Arblaster, and G. P. Compo (2003), The Asian monsoon, the tropospheric biennial oscillation, and the Indian Ocean zonal mode in the NCAR CSM, *J. Clim.*, *16*, 1617–1642, doi:10.1175/1520-0442(2003)016<1617:TAMTTB>2.0.CO;2.
- Luo, J.-J., R. Zhang, S. K. Behera, Y. Masumoto, F.-F. Jin, R. Lukas, and T. Yamagata (2010), Interaction between El Niño and extreme Indian Ocean Dipole, *J. Clim.*, *23*, 726–742, doi:10.1175/2009JCLI3104.1.
- McGregor, S., A. Timmermann, N. Schneider, M. F. Stuecker, and M. H. England (2012), The effect of the South Pacific Convergence Zone on the termination of El Niño events and the meridional asymmetry of ENSO, *J. Clim.*, *25*, 5566–5586, doi:10.1175/JCLI-D-11-00332.1.
- Meehl, G. A., and J. M. Arblaster (2002), The tropospheric biennial oscillation and Asian-Australian monsoon rainfall, *J. Clim.*, *15*, 722–744, doi:10.1175/1520-0442(2002)015<0722:TTBOAA>2.0.CO;2.
- Meehl, G. A., J. M. Arblaster, and J. Loschnigg (2003), Coupled ocean-atmosphere dynamical processes in the tropical Indian and Pacific Oceans and the TBO, *J. Clim.*, *16*, 2138–2158, doi:10.1175/2767.1.
- Nicholls, N. (1984), The Southern Oscillation and Indonesian sea surface temperature, *Mon. Weather Rev.*, *112*, 424–432.
- Nuncio, M., and X. Yuan (2015), The influence of the Indian Ocean Dipole on Antarctic sea ice, *J. Clim.*, *28*, 2682–2690, doi:10.1175/JCLI-D-14-00390.1.
- Ohba, M., and H. Ueda (2007), An Impact of SST anomalies in the Indian Ocean in acceleration of the El Niño to La Niña transition, *J. Meteorol. Soc. Jpn. Ser. II*, *85*, 335–348, doi:10.2151/jmsj.85.335.
- Philander, S. G. (1983), El Niño Southern Oscillation phenomena, *Nature*, *302*, 295–301, doi:10.1038/302295a0.
- Rayner, N. A., D. E. Parker, E. B. Horton, C. K. Folland, L. V. Alexander, D. P. Rowell, E. C. Kent, and A. Kaplan (2003), Global analyses of sea surface temperature, sea ice, and night marine air temperature since the late nineteenth century, *J. Geophys. Res.*, *108*(D14), 4407, doi:10.1029/2002JD002670.
- Saji, N. H., and T. Yamagata (2003), Possible impacts of Indian Ocean Dipole mode events on global climate, *Clim. Res.*, *25*, 151–169.
- Saji, N. H., B. N. Goswami, P. N. Vinayachandran, and T. Yamagata (1999), A dipole mode in the tropical Indian Ocean, *Nature*, *401*, 360–363.
- Song, Q., G. A. Vecchi, and A. J. Rosati (2007), Indian ocean variability in the GFDL coupled climate model, *J. Clim.*, *20*, 2895–2916, doi:10.1175/JCLI4159.1.
- Stuecker, M. F., A. Timmermann, F.-F. Jin, S. McGregor, and H.-L. Ren (2013), A combination mode of the annual cycle and the El Niño/Southern Oscillation, *Nat. Geosci.*, *6*, 540–544, doi:10.1038/ngeo1826.
- Stuecker, M. F., F.-F. Jin, A. Timmermann, and S. McGregor (2015a), Combination mode dynamics of the anomalous Northwest Pacific anticyclone, *J. Clim.*, *28*, 1093–1111, doi:10.1175/JCLI-D-14-00225.1.
- Stuecker, M. F., F.-F. Jin, and A. Timmermann (2015b), El Niño–Southern Oscillation frequency cascade, *Proc. Natl. Acad. Sci. U.S.A.*, *112*, 13,490–13,495, doi:10.1073/pnas.1508622112.
- Stuecker, M. F., A. Timmermann, J. Yoon, and F.-F. Jin (2015c), Tropospheric biennial oscillation (TBO) indistinguishable from white noise, *Geophys. Res. Lett.*, *42*, 7785–7791, doi:10.1002/2015GL065878.
- Stuecker, M. F., F.-F. Jin, A. Timmermann, and S. McGregor (2016), Reply to “Comments on ‘Combination mode dynamics of the anomalous Northwest Pacific Anticyclone’”, *J. Clim.*, *29*, 4695–4706, doi:10.1175/JCLI-D-15-0558.1.
- Webster, P. J., A. M. Moore, J. P. Loschnigg, and R. R. Leben (1999), Coupled ocean-atmosphere dynamics in the Indian Ocean during 1997–98, *Nature*, *401*, 356–360, doi:10.1038/43848.
- Wittenberg, A. T. (2009), Are historical records sufficient to constrain ENSO simulations?, *Geophys. Res. Lett.*, *36*, L12702, doi:10.1029/2009GL038710.
- Wittenberg, A. T., A. Rosati, N.-C. Lau, and J. J. Plushay (2006), GFDL's CM2 global coupled climate models. Part III: Tropical Pacific Climate and ENSO, *J. Clim.*, *19*, 698–722.
- Wittenberg, A. T., A. Rosati, T. L. Delworth, G. A. Vecchi, and F. Zeng (2014), ENSO modulation: Is it decadal predictable?, *J. Clim.*, *27*, 2667–2681, doi:10.1175/JCLI-D-13-00577.1.
- Wyrtki, K. (1985), Water displacements in the Pacific and the Genesis of El Niño Cycles, *J. Geophys. Res.*, *90*, 7129–7132.
- Xie, S.-P., H. Annamalai, F. A. Schott, and J. P. McCreary (2002), Structure and mechanisms of South Indian Ocean climate variability, *J. Clim.*, *15*, 864–878.
- Xie, S.-P., K. Hu, J. Hafner, H. Tokinaga, Y. Du, G. Huang, and T. Sampe (2009), Indian ocean capacitor effect on Indo-Western Pacific climate during the summer following El Niño, *J. Clim.*, *22*, 730–747, doi:10.1175/2008JCLI2544.1.

- Yang, Y., S.-P. Xie, L. Wu, Y. Kosaka, N.-C. Lau, and G. A. Vecchi (2015), Seasonality and predictability of the Indian Ocean dipole mode: ENSO forcing and internal variability, *J. Clim.*, *28*, 8021–8036, doi:10.1175/JCLI-D-15-0078.1.
- Zhang, W., Y. Wang, F.-F. Jin, M. F. Stuecker, and A. G. Turner (2015), Impact of different El Niño types on the El Niño/IOD relationship, *Geophys. Res. Lett.*, *42*, 8570–8576, doi:10.1002/2015GL065703.
- Zhang, W., F.-F. Jin, M. F. Stuecker, A. T. Wittenberg, A. Timmermann, H.-L. Ren, J.-S. Kug, W. Cai, and M. Cane (2016), Unraveling El Niño's impact on the East Asian monsoon and Yangtze River summer flooding, *Geophys. Res. Lett.*, *43*, 11,375–11,382, doi:10.1002/2016GL071190.